Research Papers

Distributed internal thermal monitoring of lithium ion batteries with fibre sensors

Yifei Yu [*], Timothy Vincent, Jonathan Sansom, David Greenwood, James Marco

WMG, University of Warwick, Coventry CV4 7AL, United Kingdom

A B S T R A C T

Real-time monitoring of the thermal characteristics of a lithium ion battery under electrical excitation, is a key requirement that underpins the safe operation of the battery; its reliability and life. Further, it facilitates the design of many supporting elements of the battery system, including the thermal management strategy and the algorithms that comprise the battery management system. The novelty of this study is advanced distributed thermal monitoring from external to embedded measurement for future smart battery and management. Rayleigh scattering based optical fibre sensors are known to be robust and able to operate when immersed in electrolyte, they have a small physical size and are able to provide a measurement of temperature with a spatial resolution of circa 2.6 mm. The spatial distribution of the temperature profile, arising from the complexity and variations within the cell is investigated. The results show that the peak temperature between the cell core and surface, along the cell length can be as high as 9.7 °C for 1C discharge. This paper provides a detailed explanation of the cell modification method, instrumentation process and the fundamental principles of in-cell optical measurement. Results are presented and discussed within the context of enhanced battery thermal management and improved system safety that are applicable to the application of lithium ion batteries across a number of domains including automotive and aerospace.

1. Introduction

Electric vehicles (EVs) are viewed as the future of transportation, with many countries introducing legislation to phase out traditional internal combustion engine (ICE) vehicles over the next 10–15 years. In the UK, the Government has recently accelerated plans to halt the sale of petrol and diesel fuelled passenger vehicles after 2030 [1]. In the aerospace industry, the progress towards aircraft electrification is less well advanced [2,3]. The current generation of Lithium Ion batteries (LIB) and pack designs often fall short of the energy density requirements of the sector and fail to incorporate the necessary monitoring apparatus to meet the strict status and health monitoring demands of aircraft original equipment manufacturers (OEMs) [2,3].

LIBs are the favoured cells for many automotive applications, offering approximately 230 Wh/kg energy density at a cell level, or approximately 170 Wh/kg when integrated into a vehicle pack [4].

Automotive engineers are often required to prioritise initial part and manufacturing costs at the expense of system level attributes such as the inclusion of additional sensing and control hardware – improving the observability of the system, but negatively impacting energy density and manufacturing cost [5,6]. Typically, EV battery packs contain <20 sensors to monitor often many-hundreds of individual cells [7,8]. There is growing demand for stricter regulations regarding passenger safety in EVs. For example, with the United Nations on EV safety ruling occupants should be given a five minute warning, prior to the egress of smoke or hazardous conditions manifesting within the cabin that may be a by-product of a thermal runaway or battery failure [9,10]. In the aerospace industry, regulations are likely to be even stricter, with the need to reduce the risk, during flight, of a battery thermal event. Meeting this requirement, will mandate a more robust and insightful understanding of battery temperature during operation to maintain aircraft operation. For example, in 2013, the Boeing Dreamline fleet was grounded following an incident in the auxiliary battery pack of the aircraft [11]. It

was reported that this was due to inadequate battery sensor data recordings, it was impossible to identify the specific failed cell [12], therefore prolonging the period aircraft could not fly and the disruption to the airline sector.

The design of an effective battery pack thermal management system (both heating and cooling) is regarded to be essential, to ensure pack longevity and safe operation [8,13]. The energy capacity of a poor temperature managed cell within a pack suffers from rapid degradation. For example, research has highlighted that in a stack of 5 pouch cells electrically connected in series, with over 2000 charge/discharge cycles applied, it was reported the capacity of a cell located centrally could lose almost 50% of its retained capacity. This is compared to a pouch cell at the top of the stack that received adequate cooling, loosing just 13% [14]. The internal construction of the cell itself, as well as the pack layout must be understood when designing the thermal management system [15]. For example, the design and location of the current collector tabs greatly influences the level of heat generation and dissipation. For a large format cylindrical cell, a large increase in temperature was reported when comparing a continuous tab to a two-tab (30% increased heat generation) design [16]. Poor cooling design can lead to a higher rate of performance degradation and non-uniformity within the rate of decay of individual cells within the system [13,14]. This system level heterogeneous behaviour is further compounded, where "hot-spots" are generated within the cells and battery pack that may move location, over-time, as the system is loaded and individual cells age at different rates. Thereby mandating the need to be able to measure the spatial evolution of the temperature build-up within different cells and across the complete pack. Moreover, the heat generation rate in a LIB cell and poor thermal conductivity can cause large temperature rise and thermal gradients within the cell [17]. According to the reliable temperature information, efficient ageing predictions [18], self-heating [19], electrochemical thermal modelling [20,21] and as well as charging managements of LIB [22] could be achieved and significantly benefit the development of energy storage systems.

In this work, we show our solution to the research challenge of monitoring the internal temperature of a cylindrical format 21,700 LIB cell via a distributed fibre optic sensor (DFOS) and our novel cell instrumentation methodology. Furthermore, we demonstrate the value of implementing core sensing within the cell. Results highlight that external surface measurements do not accurately quantify the amplitude and rate-of-change of battery temperature for different charge and discharge conditions.

This paper is structured as follows. Section 2 provides an overview of comparative temperature sensing methods employed within the context of LIB characterization and deployment. Section 3 introduces the materials and experimental methods associated with LIB modification, sensor insertion and experimental measurement using DFOS. Experimental results are presented in Section 4, with Further work and Conclusions discussed in Sections 5 and 6 respectively.

2. Lithium ion battery temperature sensing methods

Point temperature sensors, such as thermocouple devices, involve complex wiring requirements leading to manufacturers prioritising a reduction of cost in pack design. As thermocouples require a cold junction, they cannot be connected in series, limiting the spatial resolution of the measurement that can be achieved. These sensors are typically used in automotive applications, where the sensors can be attached to various locations within the battery pack to facilitate surface temperature measurements. However, sensors located only on the surface of a cell are not a substitute for internal temperature sensing when assessing cell degradation and performance. Rapid fluctuations in temperature resulting from transient electrical load may be missed by external sensors [5]. Additionally, slow heat dissipation (<1 W m^{-1} k^{-1} [16]) through electrode-separator plane increases the response time of sensors to temperature rise. Miniature thermocouples have been reportedly installed successfully internally within a 18,650 cell between the electrode layers [23]. These experiments demonstrated the slow transfer of heat along the radial-plane of the cell (order of 10s of seconds), and overall lower temperatures recorded. Richardson et al. performed experiments involving internal thermocouple sensors located both on the cell surface and internally within the cell housing, where between 5 °C and 10 °C hotter temperatures were reported, compared to external surface mounted sensors [5,24]. Thermocouples offer a large measurement range, but only provide point measurement capabilities, limiting the detection of internal hot spots. Localised degradation is reported as a common initiator to eventual complete failure (thermal runaway) [25]. Hot spots formation could start from a small area, e.g. 10 mm^2 [26]. High spatial resolution is vital to develop innovative cooling systems where the location and movement of the hot-spot is monitored in real-time and the cooling strategy modified accordingly [27]. Further, the construction of the cell can be analysed (to understand cooling requirements) by detailed temperature maps of internal temperature variation [28,29].

Optical fibre sensors have been identified as one means to analyse temperature and strain within LIBs [30], with a growing research field to expand their enhanced sensing capabilities. They offer attractive qualities for cell instrumentation, including immunity to electromagnetic interference and electrostatic discharge [31], robustness to harsh chemical environments, flexible installation and a small physical diameter. Fibre Bragg Grating (FBG) sensors have been noted to be the major choice for embedding sensing within LIBs, in terms of strain and temperature measurements [30]. FBG is a type of semi-distributed Bragg reflector constructed in a short segment with pre-defined location of optical fibre that reflects particular wavelengths of light [32], which is limited by the number of sensing points. FBG measurements at two locations (centre and tab electrode, between two separator layers) within a pouch cell were reported by Novais et al. [31]. During 5C and 8C cycles the internal centre sensor was found to record a peak temperature of 0.7 °C higher (relative to the tab-mounted sensor), while both internal sensors recorded circa 4 °C higher peak temperatures compared to their external counterparts. Experiments instrumenting coin cells with FBG sensors were performed by Fortier et al. [33]. Internal temperatures were found to be as great as 10 °C higher compared to external sensors, even at a low cycling rate of C/20. The construction of the coin cells is likely to slow heat dissipation, demonstrating the need for internal temperature measurements to be available to the battery management system (BMS). Under normal conditions surface temperature and internal temperature is related by the thermal mass of the cell and the thermal conduction pathways through the various layers that make-up the cell. Under failure conditions, these pathways breakdown and the core and surface temperature difference can be significant. Therefore, internal temperature monitoring of cells will aid detection of thermal events and support algorithm development. Cylindrical 18,650 cylindrical cells have previously been instrumented with single point FBG sensors, although the failed to fully exploit the temperature sensing we
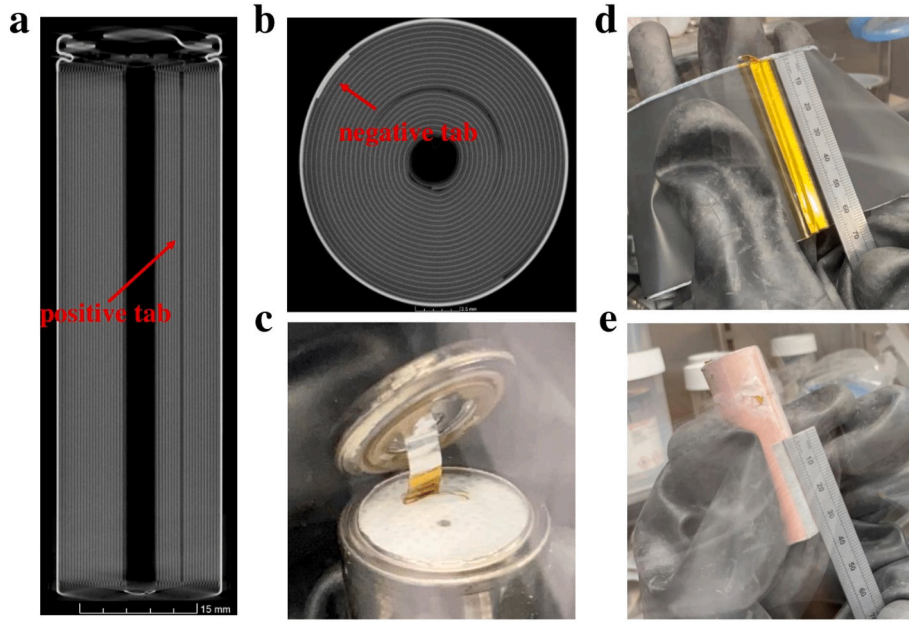
Fig. 1. Cell investigation by CT scan and cell disassembling. CT scanning before cell modification: a) front view b) middle view; c) positive terminal investigation; d) positive current tab; e) negative current tab.

report in this work [34].

For large format LIBs, distributed sensing over the whole area of the cell is highly desirable to obtain the spatially-resolved temperature distribution information for timely diagnostic of the thermal in-homogeneities [35]. In Section 3, we demonstrate a cell modification procedure and how distributed optical fibres can be employed to improve our understanding of thermal behaviour of cylindrical cells, by inserting an optical fibre packaged in a Poly-Tetra-Fluoro-Ethylene (PTFE) tube inside of the LIB. The advantages of using Rayleigh scattering based fibre optics for battery internal and external thermal measurement are their distributed sensing with high spatial resolution, which enables hermetically sealing of the cell. We have previously reported on high resolution surface temperature maps of 5 Ah pouch cells [22], demonstrating the high resolution capability associated with a Rayleigh scattering based method, whilst needing only a single connection to the measurement apparatus. The advantages of distributed fibre sensing method compared with other temperature indication methods are (1) distributed sensing with high spatial resolution (2.6 mm) and long sensing distance; (2) no need for inscribing gratings in specific locations; (3) light weight; (4) immune to electromagnetic radiation; (5) resistant to corrosion. To the best of our knowledge, this is the first time that distributed cylindrical cell internal temperature has been captured in real-time and has been reported. This in-situ and *operando* characterization techniques can provide valuable real-time information and insights on thermal behaviour, which can help researchers improve battery thermal modelling, improved diagnostics and prognostics capabilities and the design of new charge management algorithms.

3. Materials and methods

3.1. Measurement principle: distributed fibre optic sensing

When an electromagnetic wave is launched into an optical fibre, the light will be redistributed by Rayleigh scattering [36,37]. If the local change in temperature is relayed to the optical fibre, the scattered signal in the fibre will be modulated. For completeness a brief introduction can be found in [38,39]. It is noteworthy that the same experimental set-up, was employed to measure the distributed surface temperature within a

LIB pouch cell and is published in [22]. The desired features of Rayleigh scattering based fibre sensing technique allows distributed measurements with millimetre-scale spatial resolution and high measurement accuracy, making it a suitable solution for LIB *operando* and in-situ applications. Coherent Optical Frequency Domain Reflectometry (C-OFDR), a type of Rayleigh scattering based DFOS, is performed to monitor distributed temperature measurements. C-OFDR was selected due to its high spatial resolution (approx. 2.6 mm) measurement capability.

A change in local temperature from the baseline condition results in a locally-reflected frequency shift ($\Delta\nu$) in the Rayleigh spectrum of light scattered along the fibre, which can be scaled to form a distributed sensor by tuning the input frequency of the laser source. The optical fibre employed in this work is a polyimide coated optical fibre, where the physical length and index of refraction of the fibre are intrinsically sensitive to the measurement of temperature. During experimentation, the optical fibre (diameter of the optical fibre is 125 µm) is contained within a PTFE tube (diameter of the PTFE tube is 500 µm), thereby ensuring the fibre is solely a function of variations in temperature.

The locally-reflected frequency shift in the spectrum of light scattered in the DFOS in response to both strain and temperature is analogous to a shift in the spectral shift, $\Delta\nu_{DFOS}$:

$$-\frac{\Delta\nu_{DFOS}}{\nu} = K_T \Delta T_{measured} + K_\varepsilon \varepsilon_{measured} \tag{1}$$

where ν is the mean optical frequency, K_T and K_ε the temperature and strain calibration constants, $\Delta T_{measured}$ and $\varepsilon_{measured}$ are the measured temperature change and strain. In the absence of any mechanical strain, the frequency shift, $\Delta\nu_{T-DFOS}$, due to temperature variation ΔT is derived as:

$$-\frac{\Delta\nu_{T-DFOS}}{\nu} = K_T \Delta T_{measured} \tag{2}$$

The default value for germanosilicate core fibres is $K_T = 6.45 \times 10^{-6}$ °C^{-1} [36,40]. Therefore, in the absence of strain, the temperature variation ($\Delta T_{measured}$) can be defined as:

$$\Delta T_{measured} = -\frac{1}{K_T \nu} \Delta\nu_{T-DFOS} = C_T \Delta\nu_{T-DFOS} \tag{3}$$
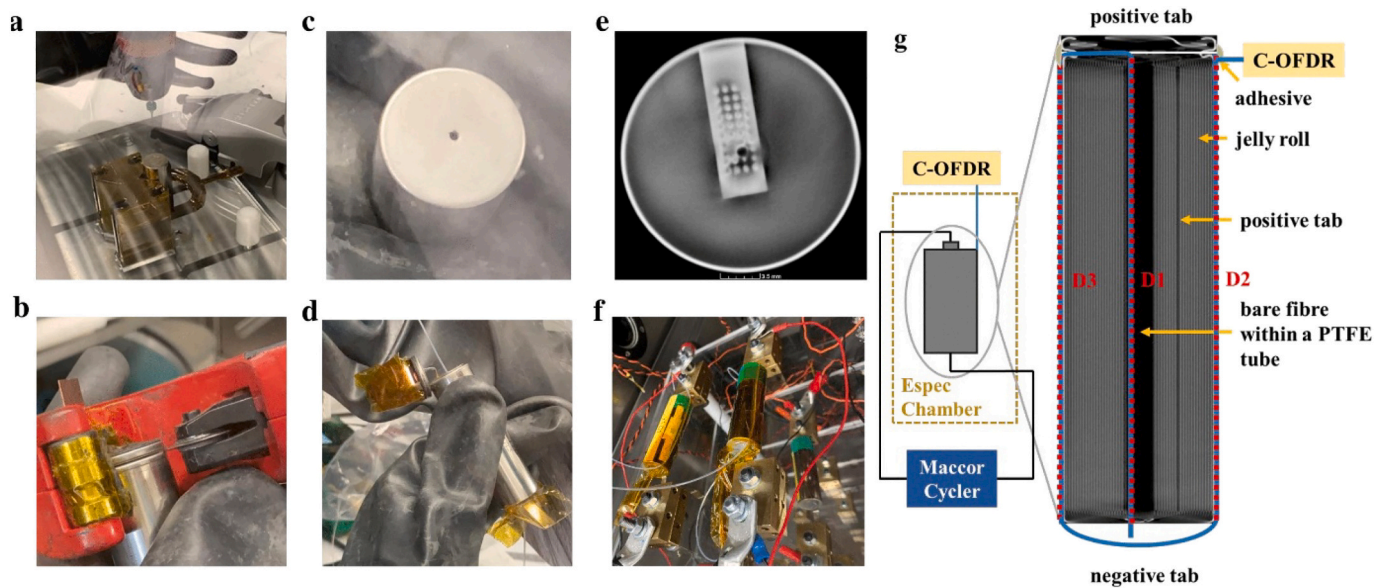
Fig. 2. Cell instrumentation process. a) hole drilling from negative terminal using a drilling machine (BOSCH PBD 40) with 1 mm drilling bit (RS); b) positive terminal opening with a pipe cutter; c) hole drilled from the negative terminal; d) optical fibre inserting from negative terminal to the positive terminal and re-sealing using Kapton tape and adhesive (Parmobond) inside an argon glove box with O_2 and H_2O concentrations of 0.1 ppm; e) negative current tab view of CT scanning after instrumentation; f) gluing the DFOS externally to the cell, placing the cell into test rig and then placing the instrumented cell into Espec thermal chamber; g) illustration of instrumented cell with optical fibre for real-time internal (D1) and external (D2 and D3) temperature monitoring.

3.2. Temperature calibration

As defined by Eq. (3), a change in the measured temperature variation ($\Delta T_{measured}$), results in a frequency shift ($\Delta \nu_{T-DFOS}$) in the Rayleigh scattering spectrum along the fibre. The distributed measure of temperature variation along the optical fibre is related to the distributed spectrum shift multiplied by the coefficient C_T with units of °C/GHz.

During the temperature sensor calibration, the optical fibre within the PTFE tube was bonded with epoxy resin to an aluminium bar, where a platinum resistance thermometer (PRT) (with an accuracy of ±0.15 °C) was placed in close physical proximity to the fibre. The calibration set-up was positioned into a Espec thermal chamber. By increasing the temperature of the thermal chamber from 5 to 55 °C with 10 °C incremental steps, the data acquisition systems for the temperature fibre sensor was set to record measurements of spectrum shift and the simultaneous measured temperature from the PRT sensor. At each temperature increment, the thermal equilibrium is defined as the output from the PRT changing less than ±0.15 °C over a 20-min time period. Once thermal equilibrium has been reached, 100 temperature readings were taken and the results indicate that a linear fit with coefficient $C_T = -0.753$ °C/GHz results in a 0.27 °C measurement deviation calculated by the 100 experimental measurements.

3.3. Cell details

Commercially available rechargeable 21,700 cylindrical LIB (model: INR21700 M50 18.20 Wh NMC 622 material) were utilised in all experiments, with 18.2 Wh nominal capacity, 3.63 V nominal average voltage, LiNiMnCoO2 cathode, graphite anode, LiPF6 in an organic solution electrolyte. As defined on the manufacturer's datasheet, the cell operates within a voltage window of 4.2 to 2.5 V. The maximum continuous charge and discharge C-rate (charge/discharge current with regard to battery nominal capacity) capabilities of the cell are 0.7C and 1.5C, respectively, where C-rate is a measure of the rate at which a battery. The cell diameter is 2.11 cm and height 7.01 cm.

3.4. Cell Instrumentation

Before cell instrumentation, a process of computerized tomography (CT) scanning, and cell disassembling were performed to understand the cell internal structure and dimensions. In this work, a TESCAN UniTOM XL system was used, while the post analysis was performed using commercially available software VGStudio Max 2.2.5. As observed from the CT scanning (Fig. 1a and b), the positive current tab is placed within the jellyroll; and the negative current tab is deposited between the jellyroll and the battery can. The diameter of the hollow of the jellyroll is approximately 3.3 mm ± 0.3 mm. The cell disassembly and instrumentation procedures were undertaken in an argon-filled glove box (Innovative Technology). After opening the positive terminal using a pipe cutter, we could observe that there is an isolator layer with a hole on the middle-top of the jellyroll (Fig. 1c). The length of the positive current tab was measured to be 6.3 cm along the jellyroll and the length of the negative current tab was measured to be 3.3 cm from the negative terminal (Fig. 1d and e respectively).

After investigating the internal physical structure of a candidate cell through CT scanning and disassembly, the remaining cells were deemed to be ready for instrumentation with an optical fibre sensor (single mode).

The first step was to fix each cell to a battery holder and drill a 0.9 mm hole into the centre of negative terminal using the drilling machine (BOSCH PBD 40) and drilling bit (RS) as shown Fig. 2a. The drilling speed was selected to be 2000 rpm, which through experimentation provided a cell-opening with the minimum of internal swarf deposition and mechanical damage to the cell can. The 0.9 mm hole in the negative terminal was sealed with Kapton tap to protect the internals of the cell.

The second stage was to open the positive terminal with a pipe cutter as illustrated in Fig. 2b. During this step, the positive terminal needs to be isolated using Kapton tape to prevent a short circuit occurring.

The third stage in the instrumentation process was to insert the optical fibre from the negative terminal through the isolation layer represented as Fig. 2c and d. The optical fibre was routed and mounted externally near to the positive current tab (D2) and negative current tab (D3) using Kapton tape as shown in Fig. 2g. The position of positive current tab and negative current were marked during CT scanning. At
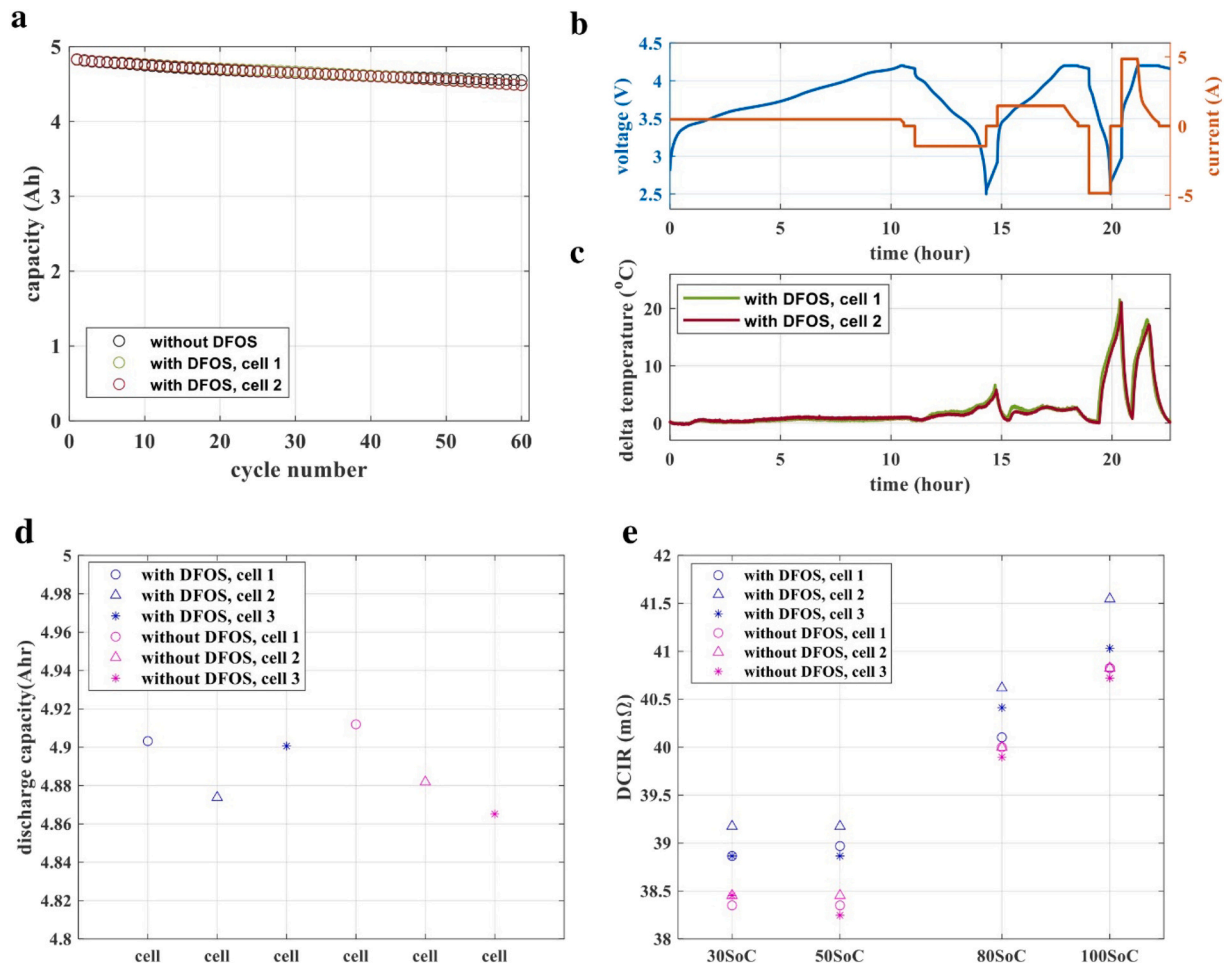
Fig. 3. **a)** Battery performance remaining unaffected after inserting the DFOS. The cells were cycled at 1C for 60 cycles; **b)** voltage and current evolution during 0.1C charge, 0.3C discharge and charge and 1C discharge and charge; **c)** maximum internal delta temperature captured by DFOS during 0.1C charge, 0.3C discharge and charge and 1C discharge and charge; **d)** discharge capacity of modified cells and non-modified cells; e) DCIR of modified cells and non-modified cells.

this stage, the positive terminal needs to be resealed using Permabond Engineering adhesives and protected using Kapton tape after the adhesive is allowed to dry.

After modification, the instrumented cell was observed through CT scanning again to ensure that the integrity of the cell, including the quality of the weld in the vicinity of the negative current tab was not compromised, as shown in Fig. 2e, which is important for mechanical integrity and to limit changes in resistance.

After cell instrumentation and re-sealing, the cell was placed in the test rig and connected to a Maccor battery cycler via copper bus bars shown as Fig. 2f. The illustration of instrumented cell is shown as Fig. 2g, where D1 measures internal temperature from the bottom (0 cm) to the top (6.3 cm) of the jellyroll with length 6.3 cm, and D2 and D3 measure external temperature near the positive current tab and negative current tab respectively with the same length of 6.3 cm.

3.5. Experimental set-up

The electrical cycling tests were performed using a Maccor battery cycler at 0.3C charge and 1C discharge respectively. The cell was placed within an Espec thermal chamber. The ambient temperature was controlled to a temperature of 25 °C. The corresponding experimental setup is illustrated in Fig. 2g. The battery cell was connected to Maccor cycler via a pair of copper bus bars in the negative and positive tabs. The DFOS was connected to the C-OFDR system, where the optical fibre performed as both the sensing media and information transmission line.

3.6. LIB test procedure

The subsequent step was the identification of the DFOS response to different electrical inputs, for this reason, the instrumented cells were subjected to a series of differing tests for different objectives of the experimental research are summarised below:

- **Characterization test**: To ensure that the fundamental characteristics of the instrumented cell (cells with DFOS) are not unduly altered, both the modified and un-modified cells underwent a rigorous characterization process. This included measuring their discharge energy capacity, direct current internal resistance (DCIR) at 30, 50, 80 and 100 State of Charge (SoC) and degradation at 25 °C ambient temperature. We conducted the characterization test on 3 instrumented and 3 non-instrumented cells. The DCIR was measured by pulse discharging the cells using 2C for 30 s. Two instrumented cells and a pristine cell were cycled using 0.3C constant current constant voltage (4.2 V) (CC-CV) charge with a cut-off current of 50 mA and 0.3C constant current (CC) discharge with a cut-off voltage of 2.5 V for 60 cycles.
- **Repeatability test**: To quantify the repeatability of temperature collected by the instrumented cells at 25 °C ambient temperature. Two instrumented cells were charged using 0.1C CC-CV charge, 0.3C CV discharge, 0.3 CC-CV charge, 1C CV discharge and 1C CC-CV discharge consecutively with a 30 min rest period between cycle.

Table 1

Characterization tests of three instrumented cells and three non-instrumented cells regarding their capacity and DCIR after instrumentation to characterize the influence of modification.

| Measured parameters	With DFOS, cell 1	With DFOS, cell 2	With DFOS, cell 3	Mean value/standard deviation	Without DFOS, cell 1	Without DFOS, cell 2	Without DFOS, cell 3	Mean value/standard deviation
Capacity (Ah)	4.90	4.87	4.90	4.89/0.0132	4.91	4.88	4.87	4.89/0.019
DCIR@30SoC (mΩ)	38.87	39.18	38.87	38.97/0.15	38.35	38.45	38.45	38.42/0.05
DCIR@50SoC (mΩ)	38.97	39.18	38.87	39.00/0.13	38.35	38.45	38.25	38.35/0.08
DCIR@80SoC (mΩ)	40.10	40.62	40.41	40.38/0.21	40.00	40.00	39.90	39.97/0.05
DCIR@100SoC (mΩ)	40.82	41.55	41.03	41.13/0.30	40.82	40.82	40.72	40.79/0.05
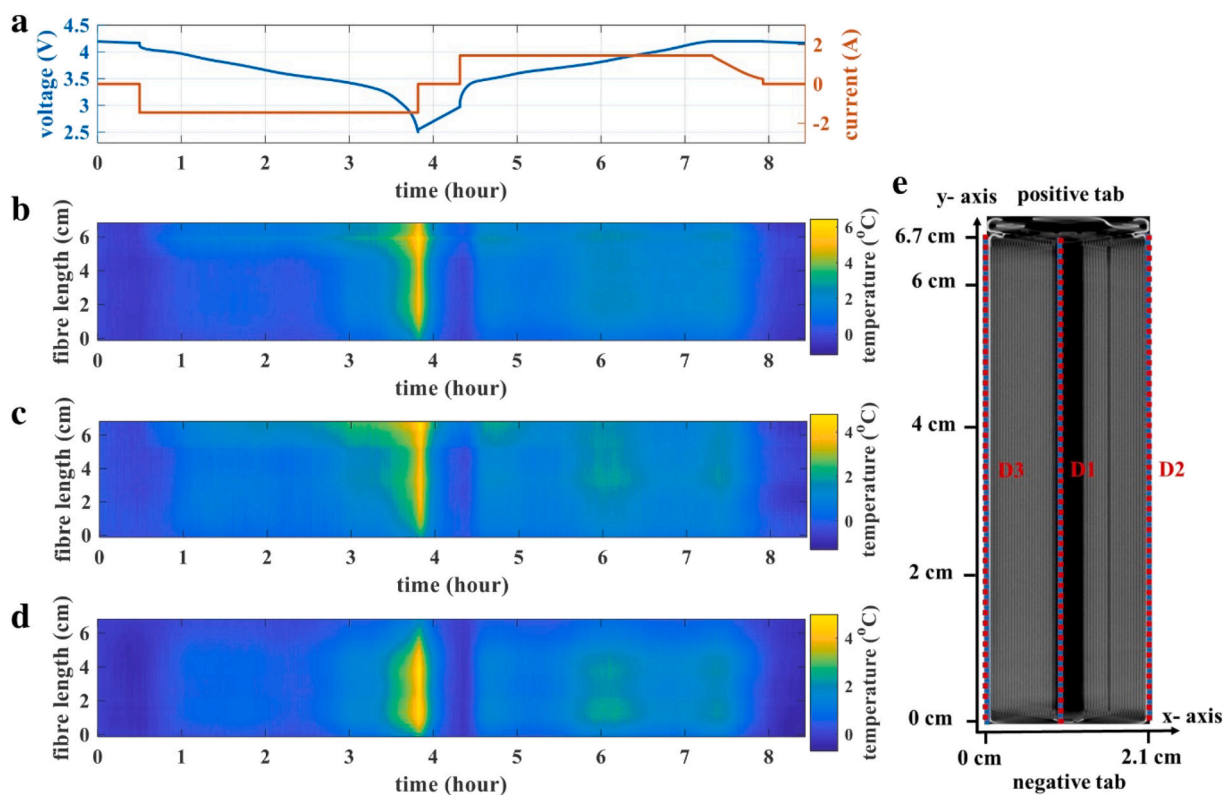
Fig. 4. 0.3C CC discharge and 0.3C CC-CV charge over time revolution in 25 °C ambient temperature with cell distributed internal and external temperature measured by DFOS; **a)** current and voltage; **b)** internal temperature distribution evolution (D1); **c)** external temperature distribution evolution (D2); **d)** external temperature distribution evolution (D3); **e)** illustration of instrumented cell.

The distributed internal and external temperature were collected during the repeatability test.

- **Electrochemical test**: To compare the internal temperature distribution with external temperature distribution at 0.3C and 1C charge and discharge respectively at 25 °C ambient temperature. After the characterization and repeatability test, a cell was discharged and charged using 0.3 and 1C CC-CV charge with a constant voltage of 4.2 V and a cut-off current of 50 mA and CC discharge with a cut-off voltage of 2.5 V respectively for a cycle with temperature collected by DFOS in real time.

4. Results and discussion

4.1. Cell characterisation and repeatability assessment

Fig. 3 compares the characterization and repeatability tests for the instrumented cells and non-instrumented cells to highlight that the DFOSs do not adversely affect the cell electrochemical properties. Fig. 3a

compares capacity retention up to 60 cycles of the pristine (without DFOS) and instrumented cells (with DFOS). The results show that the capacity of the pristine cell after 60 cycles is 4.54 Ah and the capacity of the instrumented cells is 4.48 Ah and 4.49 Ah respectively, which indicates that the DFOSs do not negatively impact the cell's electrochemical properties.

Fig. 3c shows the variation of the maximum temperature difference (temperature difference comparing with initial temperature) collected by the DFOS as a function of time-resolved voltage and current (Fig. 3b) for two instrumented cells collected in an operando mode. The results show that they maximum temperature difference of the two cells nearly superimpose with each other, indicating the reproducibility and robustness of our sensor-instrumentation method together with the reliability of the sensing signals.

For the characterization tests, there were three pristine cells and three instrumented cells tested for their capacity and DCIR at 30, 50, 80 and 100 SoC, shown as Fig. 3d and e respectively. The results further show that the instrumentation for three cells did not influence their
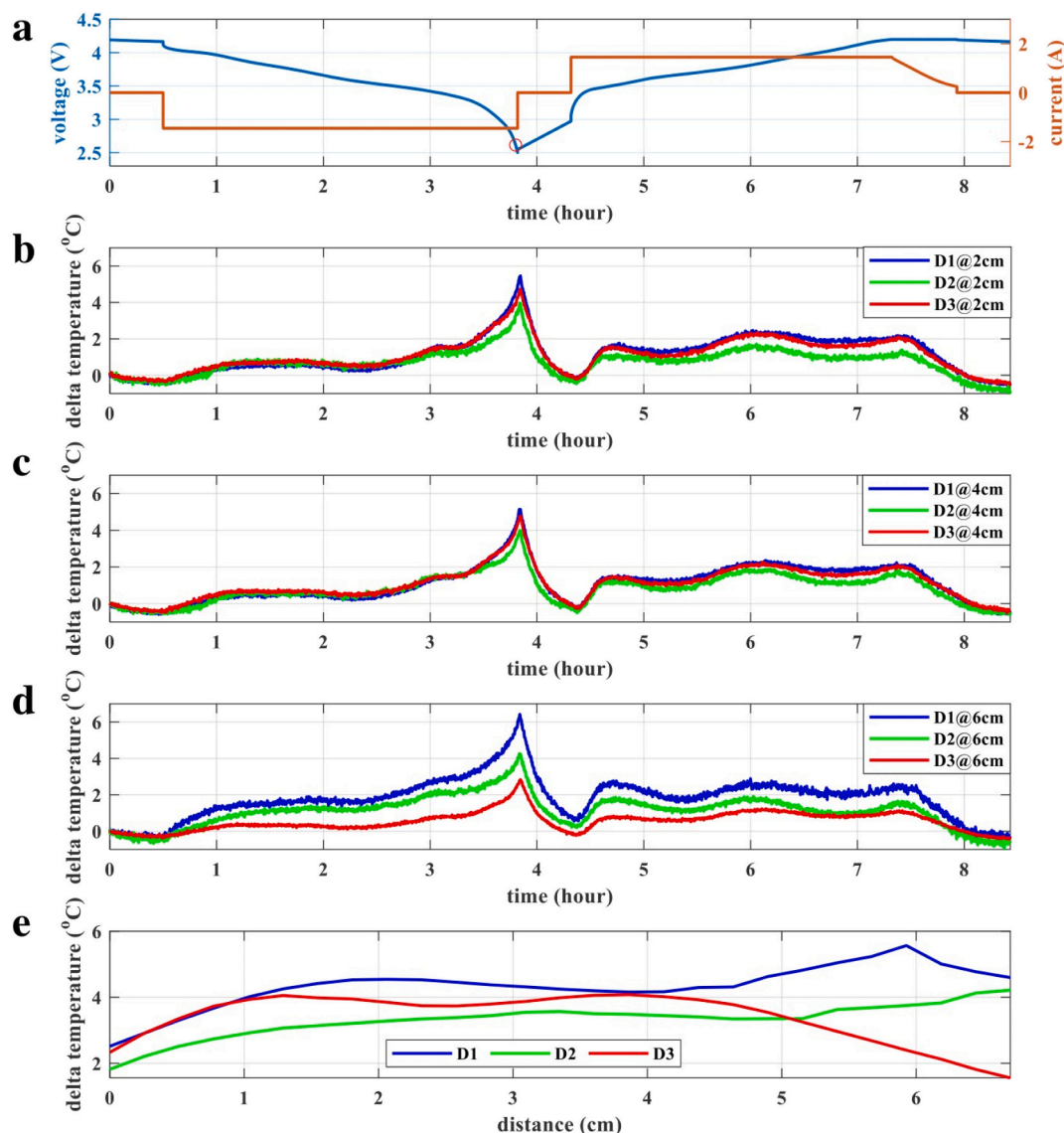
Fig. 5. 0.3C CC discharge and CC-CV charge over time revolution in 25 °C ambient temperature with cell distributed internal and external temperature measured by DFOS over a time revolution. A) Current and voltage. B) delta temperature measured by D1, D2 and D3 at 2 cm from the negative terminal; c) delta temperature measured by D1, D2 and D3 at 4 cm from the negative terminal; d) delta temperature measured by D1, D2 and D3 at 6 cm from the negative terminal; e) distribution temperature over distance of D1, D2 and D3 when the cell is fully discharged located as the red circle in a). (For interpretation of the references to colour in this figure legend, the reader is referred to the web version of this article.)

energy capacity. However, a marginal increase in DCIR at 30, 50, 80 and 100 SoC is noted within the modified cells.

Experimental results for DCIR and energy capacity are tabulated in Table 1 to further help quantify the change in cell characteristics after insertion of the DFOS.

4.2. Quantifying the internal temperature distribution within the cell

After demonstrating the repeatability of the measurements and that the cells are fundamentally unchanged, the cells were cycled using 0.3C and 1C for CV discharge and CC-CV charge with a 30 min rest interval to represent standard cycling and fast charging for the 21,700 cylindrical cells. Fig. 4 shows the internal temperature distribution D1 (Fig. 4b), external temperature distribution near the positive current tab D2 (Fig. 4c) and external temperature distribution near the negative current tab D3 (Fig. 4d). The results are shown synchronised with the voltage and current profiles in (Fig. 4a). The schematic of the instrumented cell with dimension and direction is illustrated in Fig. 4e, where the full

measurement length of the DFOS for D1, D2 and D3 are 6.7 cm in the direction from the negative terminal to the positive terminal. A spatial measurement resolution of 2.6 mm resolution is achieved along the y-axis (fibre length) in the Fig. 4b, c and d.

It is observed from Fig. 4b, c and d that the temperature for D1, D2 and D3 are not uniformly distributed. The internal temperature (D1) reaches the maximum temperature difference of 6.4 °C at 5.93 cm from the negative terminal when the cell is fully discharged. In the same time, D2 peaked its delta-temperature 4.8 °C at 6.7 cm and D3 reaches its peak temperature difference 4.9 °C at 3.6 cm from the negative terminal. The external DFOS sections (D2 and D3) reached their maximum temperatures at different locations along the cell length. This could be due to the physical non-uniform structure of the cylindrical cell, where D2 is near to the positive tab and D3 is near to the negative tab. As observed, the measured temperature of D2 indicates that the surface area near the positive tab was hotter as it gets closer to the positive terminal. This is due to the heat generated by the positive tab during discharge. Conversely, the surface area near the negative tab (D3) shows a higher
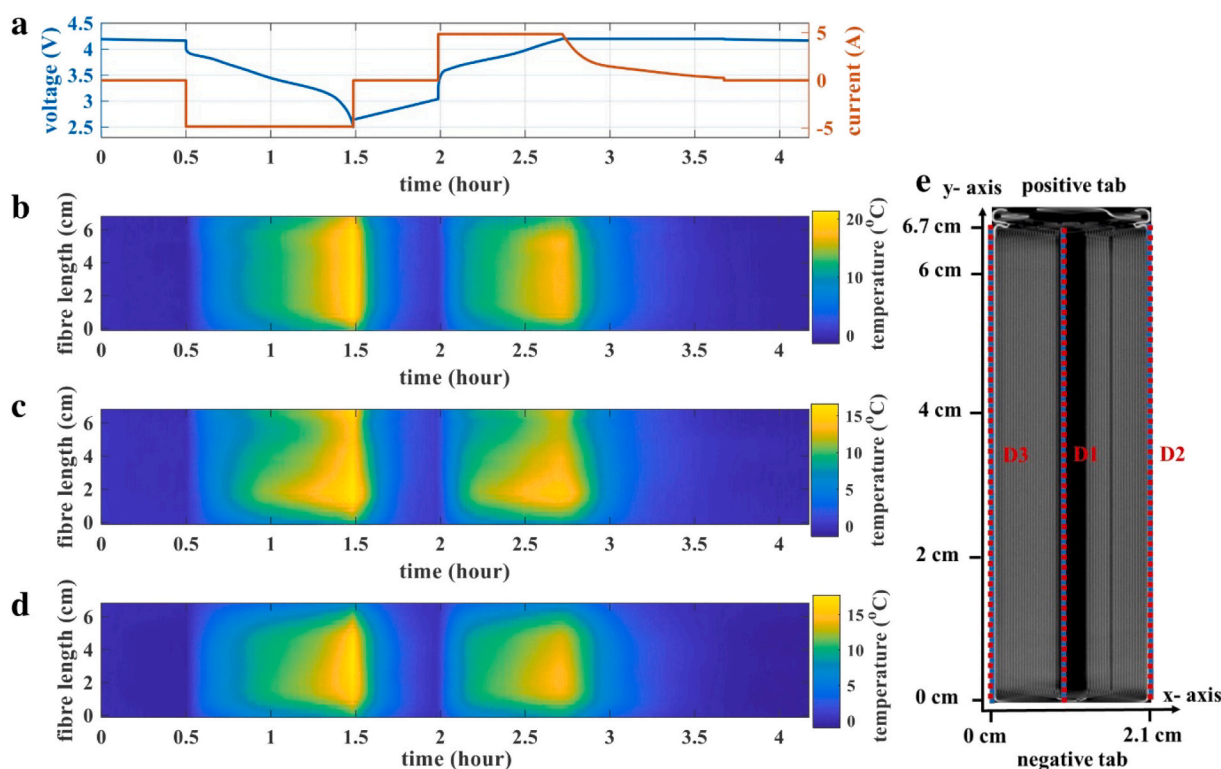
Fig. 6. 1C CC discharge and 1C CC-CV charge over time revolution in 25 °C ambient temperature with cell distributed internal and external temperature measured by DFOS; a) current and voltage; b) internal temperature distribution evolution (D1); c) external temperature distribution evolution (D2); d) external temperature distribution evolution (D3); **e**) illustration of instrumented cell.

temperature in the bottom area of the cylindrical cell due to the half-length of the negative tab from the bottom of the can. The measured internal temperature is found to be higher than the external temperature and the temperature difference (the difference between internal temperature and external temperature along the perpendicular radial axis) is location dependent due to the non-uniform structure of cylindrical cell. The internal temperature reaches its peak in the location near the positive terminal and another higher temperature area is near the bottom of the cell located around 2 cm from the bottom of the can. During 0.3C CV discharge and CC-CV charge, the maximum instantaneous temperature difference of D1, D2 and D3 are 3.4 °C, 2.8 °C and 3.1 °C respectively. As observed from Fig. 4 regarding internal and external temperature distribution, the internal temperature is higher than the surface temperature during normal C-rate cycling (0.3C) and the temperature distribution is location dependent due to the non-uniform cylindrical cell structure.

Fig. 5b, c and d shows the temperature measured by DFOS at 2 cm, 4 cm and 6 cm from the negative terminal of D1, D2 and D3 respectively for a more direct comparison between the internal and surface temperatures at different locations. At location 2 cm and 4 cm as illustrated in the Fig. 5b and c, it is observed that the internal (D1) and external (D2 and D3) show a similar temperature value and trend during the 0.3C discharge until the voltage reaches 3.3 V. At this voltage, the surface temperature (D2) starts to exhibit a lower value compared with the internal (D1) and surface temperature (D3). At location 6 cm as shown in Fig. 5d, the internal temperature (D1) shows a higher temperature and temperature gradient compared with surface temperatures (D2 and D3) during the entire 0.3C discharge and charge. Internal temperature (D1) and external temperature (D2 and D3) peak when the cell is fully discharged at 6.4 °C, 4.3 °C and 2.8 °C respectively for D1, D2 and D3. Fig. 5e represents a snapshot of the temperature distribution of D1, D2 and D3 when the cell is discharged to 2.6 V. Under this condition the internal temperature (D1) is higher than surface temperature (D2 and

D3) and the temperature difference between internal and surface temperature at the same location (y-axis) is location dependent, where the maximum temperature difference (3.2 °C) is measured between D1 (5.6 °C) and D3 (2.4 °C) at location 5.9 cm. Therefore, even using the manufacturer recommended C-rate, the measured internal and surface temperature distribution is not uniform and the temperature difference between internal and external measurements is also not consistent. With peaks of 3.6 °C at location 5.9 cm between D1 and D3, indicating that distributed temperature can provide a true real-time thermal mapping for the cylindrical cell.

Fig. 6 shows the evolution of the internal (D1) and surface (D2 and D3) temperature distribution synchronised with current and voltage (Fig. 6a) during 1C CV discharge and 1C CC-CV charge. As observed in Fig. 6b, the internal temperature difference shows a more uniform format compared with the 0.3C cycling condition. During this test case, the middle of the cell is hotter than the positive and negative terminals, with a more uniform profile compared with surface temperature measurements (D2 and D3). Comparing Fig. 6c with Fig. 5c, there is another peak of temperature difference occurring during high C-rate discharge and charge conditions, which are positioned approximately 2 cm from the negative terminal. This is in addition to the peak close to the positive tab during standard cycling (0.3C cycling). For the surface temperature (D3) distribution during 1C cycling, it shows a similar profile when comparing the distribution during 0.3 cycling, where the higher temperature measurements are located around the centre of the cell near the negative terminal, but with a higher temperature gradient. During a 1C CV discharge and CC-CV charge, the maximum temperature variation of D1, D2 and D3 are 21.3 °C at location 2.6 cm from the negative terminal, 16.6 °C at location 1.8 cm and 17.7 °C at the location 3.4 cm respectively when the cell is fully discharged. The maximum instantaneous temperature difference of D1, D2 and D3 are 6.9 °C, 7.3 °C and 9.5 °C respectively during 1C discharge. The maximum temperature difference at the same location between D1-D2 and D1-D3 is 7.5 °C at 0.8 cm and
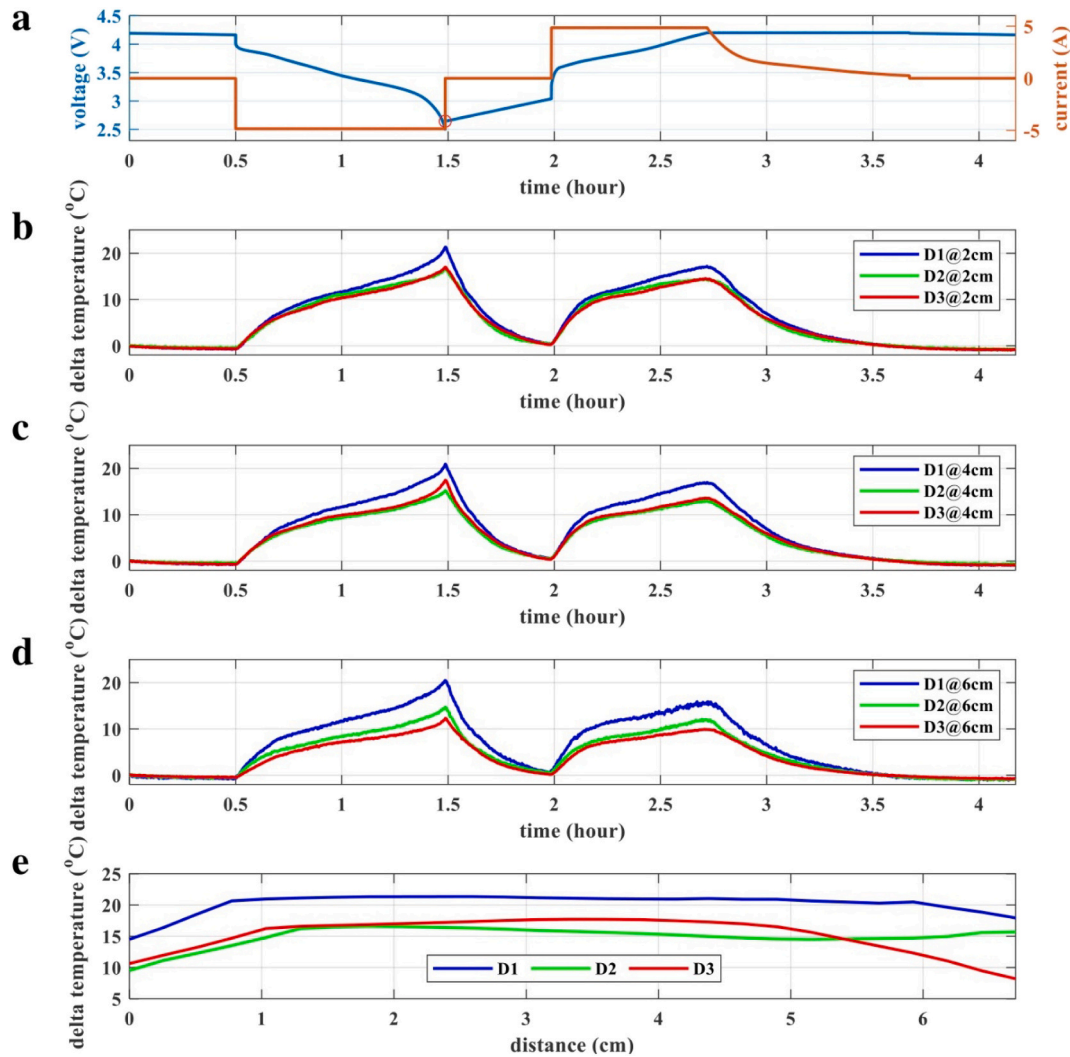
Fig. 7. 1C CC discharge and CC-CV charge over time revolution in 25 °C ambient temperature with cell distributed internal and external temperature measured by DFOS over a time revolution; a) current and voltage. b) delta temperature measured by D1, D2 and D3 at 2 cm from the negative terminal; c) delta temperature measured by D1, D2 and D3 at 4 cm from the negative terminal; d) delta temperature measured by D1, D2 and D3 at 6 cm from the negative terminal; e) distribution temperature over distance of D1, D2 and D3 when the cell is fully discharged located as the red circle in a). (For interpretation of the references to colour in this figure legend, the reader is referred to the web version of this article.)

9.7 °C at location 6.7 cm respectively during 1C discharge. This further reinforces the results that highlight the temperature difference between the cell core and surface is location dependant along the length of the cell's aluminium can.

For a direct illustration of the core and surface temperature at various locations, Fig. 7b, c and d shows the core and surface temperatures collected at the location 2 cm, 4 cm and 6 cm respectively synchronised with voltage and current (Fig. 7a). As shown in Fig. 7b and c, the temperature collected at D2 and D3 at location 2 cm and 4 cm almost superimpose with each other during a 1C CV discharge and 1C CC-CV charge. Conversely, the temperature collected by D1 at 2 cm and 4 cm always shows a higher value and higher gradient profile compared with surface temperature measurements. When the sensing location moves to 6 cm from the negative terminal, the temperature difference between core and surface becomes more apparent, where the maximum temperature difference peaks at 20.5 °C (D1), 14.7 °C (D2), and 12.3 °C (D3) when the cell is fully discharged. When the cell is discharged to 2.5 V, the instantaneous temperature distribution of the cell core and cell surface are plotted in Fig. 7e. The temperature of D2 and D3 almost superpose with each other from the negative terminal to the location near to 2.5 cm and from 2.5 cm to the positive terminal. The temperature

distribution profile of D2 and D3 illustrate a different value and trend due to the physical structure of the cell. At the same time, the temperature distribution of the core exhibits a more symmetrical profile compared with D2 and D2 and the core temperature measurements collected during 0.3C electrical cycling. From Fig. 7e, it is observed that the temperature difference at between core (D1) and surface (D2 and D3) are location dependent, where the temperature difference between D1 and D2 decreases when the location is gets closer to the positive tab. In addition, the temperature difference between D1 and D3 increases at the same time. As a summary, due to the non-uniform physical structure of the cylindrical cell, the core and surface temperature distributions vary when the C-rate differs from 0.3C to 1C, where the maximum core and surface temperature difference changes from 3.2 °C to 9.7 °C, the maximum instantaneous internal temperature difference varies from 3.4 °C to 6.9 °C, and the maximum instantaneous surface temperature difference varies from 3.1 °C to 9.5 °C.

5. Future work

In this study, we mounted two lines of optical fibre externally to the cells, close to the positive and negative tabs, other profiles of fibre

deployment with different objectives may be investigated as future work. The measurement method described here is believed to be agnostic of cell chemistry. Therefore, the transferability of these techniques to other cell formats and chemistries to further quantify the potential advantage of using DFOS to define internal and external parameters is the subject of ongoing and future work. Moreover, the intrinsic chemical, mechanical and thermal robustness of Rayleigh scattering based optical fibre sensors suggests that the in-situ thermal monitoring techniques explored here can be extended to other energy storage devices, such as fuel cells and super-capacitors, to achieve fundamental advancements in device characterization and management. Within the context of BMS integration, the optics may be integrated with the BMS hardware or be installed within the final application and communicate with the BMS via an appropriate network technology. Volume manufacturing of the instrumented cells will also be an important area to investigate as the research progresses. Key to this research is a robust methodology for instrumented cell manufacture and confirmation that DFOS insertion does not negatively impact LIB performance or life.

6. Conclusions

Through the use of Rayleigh scattering based distributed optical fibre sensor, we demonstrate cylindrical cell core and surface full temperature distribution measurement with a high spatial resolution and high temperature accuracy in operando mode. The experimental results presented demonstrate the importance and necessity of cell core and surface thermal sensing to fully quantify battery performance. In additional, the need to understand the spatial distribution of the temperature profile, arising from the complexity and variations within the cell is further highlighted. Results show that the peak temperature between the cell core and surface, along the cell length can be as high as 9.7 °C for a C-rate discharge of 1C. Conversely as the cell is fully charged, the location of the hottest location within the cell structure may move from 2.6 cm from the negative tab to 4.9 cm. In general, results show the advance and novelty of this study compared with previous published point-measurement that the proposed cell modification and instrumentation methods can measure cell distributed temperature difference and gradient for any core and surface without pre-selecting the sensing locations, which is important due to the intrinsic temperature gradient and different rate of thermal response. This has the advantage that during both characterization and deployment, the temperature within the cell and the in particular the hottest location within the cell core and on the surface can be fully quantified irrespective of the level of electrical excitation and SoC, which can be further extended in numerous applications, such as thermal monitoring and earlier warning for thermal runaway, monitoring cooling system with real-time feedbacks and optimizing battery management system.

CRediT authorship contribution statement

Yifei Yu: conceptualization, methodology, data curation, writing-original draft preparation, visualization, investigation, formal analysis, writing- reviewing and editing. Timothy Vincent: writing- reviewing and editing. Jonathan Sansom: investigation. David Greenwood: conceptualization, supervision and resources. James Marco: conceptualization, investigation, supervision, writing- reviewing and editing.

Declaration of competing interest

The authors declare that they have no known competing financial interests or personal relationships that could have appeared to influence the work reported in this paper.

References

[1] Department for Transport, The Road to Zero, London, 2018.

[2] R. Berger, Aircraft Electrical Propulsion - The Next Chapter of Aviation?, 2017.

[3] B.P.J. Ansell, K.S. Haran, Electrified airplanes, IEEE Electrif. Mag. 8 (2020) 18–26.

[4] A. Misra, Energy storage for electrified aircraft, IEEE Electrif. Mag. 6 (2018) 54–61.

[5] R.R. Richardson, S. Zhao, D.A. Howey, On-board monitoring of 2-D spatially-resolved temperatures in cylindrical lithium-ion batteries: part II. State estimation via impedance-based temperature sensing, J. Power Sources 327 (2016) 726–735.

[6] A. Kwade, W. Haselrieder, R. Leithoff, A. Modlinger, F. Dietrich, K. Droeder, Current status and challenges for automotive battery production technologies, Nat. Energy 3 (2018) 290–300.

[7] X. Lin, H.E. Perez, J.B. Siegel, A.G. Stefanopoulou, Robust estimation of battery system temperature distribution under sparse sensing and uncertainty, IEEE Trans. Control Syst. Technol. 28 (2020) 753–765.

[8] T. Grandjean, A. Barai, E. Hosseinzadeh, Y. Guo, A. McGordon, J. Marco, Large format lithium ion pouch cell full thermal characterisation for improved electric vehicle thermal management, J. Power Sources 359 (2017) 215–225.

[9] T. Cai, P. Valecha, V. Tran, B. Engle, A. Stefanopoulou, J. Siegel, Detection of li-ion battery failure and venting with carbon dioxide sensors, ETransportation 7 (2021), 100100.

[10] J. Mertens, A. Börger, Generic hazard and risk assessment for warning and intervention systems for thermal propagation, ATZelectronics Worldw. 15 (2020) 52–55.

[11] N. Williard, W. He, C. Hendricks, M. Pecht, Lessons learned from the 787 dreamliner issue on lithium-ion battery reliability, Energies 6 (2013) 4682–4695.

[12] M.K. Tran, M. Fowler, A review of lithium-ion battery fault diagnostic algorithms: current progress and future challenges, Algorithms 13 (2020).

[13] E. Hosseinzadeh, S. Arias, M. Krishna, D. Worwood, A. Barai, D. Widanalage, J. Marco, Quantifying cell-to-cell variations of a parallel battery module for different pack configurations, Appl. Energy 282 (2021), 115859.

[14] G.M. Cavalheiro, T. Iriyama, G.J. Nelson, S. Huang, G. Zhang, Effects of nonuniform temperature distribution on degradation of lithium-ion batteries, J. Electrochem. Energy Convers. Storage 17 (2020).

[15] H. Liu, Z. Wei, W. He, J. Zhao, Thermal issues about li-ion batteries and recent progress in battery thermal management systems: a review, Energy Convers. Manag. 150 (2017) 304–330.

[16] K.J. Lee, K. Smith, A. Pesaran, G.H. Kim, Three dimensional thermal-, electrical-, and electrochemical-coupled model for cylindrical wound large format lithium-ion batteries, J. Power Sources 241 (2013) 20–32.

[17] V. Vishwakarma, C. Waghela, Z. Wei, R. Prasher, S.C. Nagpure, J. Li, F. Liu, C. Daniel, A. Jain, Heat transfer enhancement in a lithium-ion cell through improved material-level thermal transport, J. Power Sources 300 (2015) 123–131.

[18] K. Purohit, S. Srivastava, V. Nookala, V. Joshi, P. Shah, R. Sekhar, S. Panchal, M. Fowler, R. Fraser, M.K. Tran, C. Shum, Soft sensors for state of charge, state of energy and power loss in formula student electric vehicle, Appl. Syst. Innov. 4 (2021) 1–27.

[19] C. Akkaldevi, S.D. Chitta, J. Jaidi, S. Panchal, M. Fowler, R. Fraser, Coupled electrochemical-thermal simulations and validation of minichannel cold-plate water-cooled prismatic 20 Ah LiFePO4 battery, Electrochem. 2 (2021) 643–663.

[20] V.G. Choudhari, A.S. Dhoble, S. Panchal, M. Fowler, R. Fraser, Numerical investigation on thermal behaviour of 5 × 5 cell configured battery pack using phase change material and fin structure layout, J. Energy Storage 43 (2021), 103234.

[21] S.D. Chitta, C. Akkaldevi, J. Jaidi, S. Panchal, M. Fowler, R. Fraser, Comparison of lumped and 1D electrochemical models for prismatic 20Ah LiFePO4 battery sandwiched between minichannel cold-plates, Appl. Therm. Eng. 199 (2021), 117586.

[22] Y. Yu, E. Vergori, D. Worwood, Y. Tripathy, Y. Guo, A. Somá, D. Greenwood, J. Marco, Distributed thermal monitoring of lithium ion batteries with optical fibre sensors, J. Energy Storage 39 (2021).

[23] G. Zhang, L. Cao, S. Ge, C.-Y. Wang, C.E. Shaffer, C.D. Rahn, In situ measurement of radial temperature distributions in cylindrical li-ion cells, J. Electrochem. Soc. 161 (2014) A1499–A1507.

[24] R.R. Richardson, P.T. Ireland, D.A. Howey, Battery internal temperature estimation by combined impedance and surface temperature measurement, J. Power Sources 265 (2014) 254–261, https://doi.org/10.1016/j.jpowsour.2014.04.129.

[25] Y. Liu, P. Sun, H. Niu, X. Huang, G. Rein, Propensity to self-heating ignition of open-circuit pouch lithium-ion battery pile on a hot boundary, Fire Saf. J. 103081 (2020).

[26] D.P. Finegan, J. Darst, W. Walker, Q. Li, C. Yang, R. Jervis, T.M.M. Heenan, J. Hack, J.C. Thomas, A. Rack, D.J.L. Brett, P.R. Shearing, M. Keyser, E. Darcy, Modelling and experiments to identify high-risk failure scenarios for testing the safety of lithium-ion cells, J. Power Sources 417 (2019) 29–41.

[27] P.J. Osswald, S.V. Erhard, A. Noel, P. Keil, F.M. Kindermann, H. Hoster, A. Jossen, Current density distribution in cylindrical Li-ion cells during impedance measurements, J. Power Sources 314 (2016) 93–101.

[28] J. Jaguemont, A. Nikolian, N. Omar, S. Goutam, J. Van Mierlo, P. Van Den Bossche, Development of a two-dimensional-thermal model of three battery chemistries, IEEE Trans. Energy Convers. 32 (2017) 1447–1455.

[29] Z. Wang, J. Ma, L. Zhang, Finite element thermal model and simulation for a cylindrical Li-ion battery, IEEE Access 5 (2017) 15372–15379.

[30] Z. Wei, J. Zhao, H. He, G. Ding, H. Cui, L. Liu, Future smart battery and management: advanced sensing from external to embedded multi-dimensional measurement, J. Power Sources 489 (2021), 229462.

[31] S. Novais, M. Nascimento, L. Grande, M. Domingues, P. Antunes, N. Alberto, C. Leitão, R. Oliveira, S. Koch, G. Kim, S. Passerini, J. Pinto, Internal and external temperature monitoring of a Li-ion battery with fiber bragg grating sensors, Sensors 16 (2016) 1394.

[32] K.O. Hill, G. Meltz, Fiber bragg grating technology fundamentals and overview, J. Light. Technol. 15 (1997) 1263–1276.

[33] A. Fortier, M. Tsao, N.D. Williard, Y. Xing, M.G. Pecht, Preliminary study on integration of fiber optic bragg grating sensors in li-ion batteries and in situ strain and temperature monitoring of battery cells, Energies 10 (2017).

[34] E. McTurk, T. Amietszajew, J. Fleming, R. Bhagat, Thermo-electrochemical instrumentation of cylindrical Li-ion cells, J. Power Sources 379 (2018) 309–316.

[35] Z. Li, J. Zhang, B. Wu, J. Huang, Z. Nie, Y. Sun, F. An, N. Wu, Examining temporal and spatial variations of internal temperature in large-format laminated battery with embedded thermocouples, J. Power Sources 241 (2013) 536–553.

[36] M. Froggatt, J. Moore, High-spatial-resolution distributed strain measurement in optical fiber with Rayleigh scatter, Appl. Opt. 37 (1998) 1735–1740.

[37] B. Lee, Review of the present status of optical fiber sensors, Opt. Fiber Technol. 9 (2003) 57–79.

[38] D.E.N. Davies, Fiber Optic Sensors: An Untroduction for Engineers and Scientists, Second edi, 2011.

[39] G. Rajan, Optical Fiber Sensors: Advanced Techniques and Applications, 2015.

[40] S.T. Kreger, D.K. Gifford, M.E. Froggatt, B.J. Soller, M.S. Wolfe, High resolution distributed strain or temperature measurements in single- and multi-mode fiber using swept-wavelength interferometry, Opt. InfoBase Conf. Pap. (2006), https://doi.org/10.1364/OFS.2006.ThE42.